Phase Diagram of Magnetic Nanodisks measured by SEMPA

S.-H. Chung[1,2], R. D. McMichael[1], D. T. Pierce[1], and J. Unguris[1]
[1] *Center for Nanoscale Science and Technology, NIST, Gaithersburg, MD 20899 and*
[2] *Maryland NanoCenter, University of Maryland, College Park, MD 20742*
(Dated: June 19, 2009)

We use Scanning Electron Microscopy with Polarization Analysis (SEMPA) to image the magnetic domain structures of *individual* ferromagnetic nanodisks with different diameters and thicknesses, and thereby determine the phase diagram of the magnetic ground states in these technologically important magnetic structures. Depending on the nanodisk dimensions, we observe magnetic structures based on one of three configurations: a single domain in-plane, a single domain out-of-plane, or a vortex state. By systematically imaging $Ni_{80}Fe_{15}Mo_5$ nanodisks with diameters that range from 35 nm to 190 nm and with thicknesses that range from 10 nm to 65 nm, we are able to locate phase boundaries between the three different phases and the triple point. The phase boundaries are not sharply defined, however. Near the boundaries, we observe disks in a mixture of the different, metastable ground phases, and we observe variations of the basic states, such as a tilted vortex configuration. A magnetic phase diagram generated by a micromagnetic simulation is found to be in good qualitative agreement with the phase diagram determined by the SEMPA measurements. Determining the magnetic phases in the sub-100 nm nanodisks enables tailoring material properties and geometry of nanodisks for various potential applications.

PACS numbers:

I. INTRODUCTION

The behavior of magnetic nanostructures is technologically important for possible applications[1] such as magnetic data storage[2], magnetic memory[3] and spintronic devices.[4] In particular, magnetic *nanodisks* of soft ferromagnetic materials with sizes less than 100 nm are of recent interest not only due to the challenges in lithography and measurement but also due to their unique magnetic properties compared to micron size or bulk state magnets. In the sub-100 nm size range, the energy cost to support domain walls and multidomain structures becomes prohibitive and the magnetization configuration of many magnetic materials favors a single domain state. 'Single domain' in this context does not necessarily mean uniform magnetization, however. Especially for soft magnetic materials, the magnetization typically has non-uniformities such as curling near surfaces and edges, due to non-uniform dipolar fields.[5,6]

Depending on aspect ratio (thickness/diameter), the magnetic configuration of nanodisks with dimensions less than 100 nm is based on one of three ground states: a single domain in-plane state, a single domain out-of-plane state or a vortex state as illustrated in Fig. 1.[7] Nanodisks with a low aspect ratio form single domain in-plane states and nanodisks with a high aspect ratio form single domain out-of-plane states. Nanodisks with an intermediate aspect ratio and diameter several times larger than the magnetic exchange length $l_{ex} = \sqrt{2A/\mu_0 M_s^2}$ (A: exchange stiffness, M_s: the saturation magnetization) form in-plane flux closure states or magnetic vortex states. In the vortex state, the magnetization forms a flux-closed loop following the circumference of the disk, and turns toward the surface normal of either the top or bottom of the disk in the vortex core, which typically has a lateral size of a few times l_{ex}. Vortices are characterized by two parameters, chirality and polarity. Chirality is the sense of the in-plane flux closure and is either clockwise or counter-clockwise. Chirality determines the direction of the vortex core motion under a dc magnetic field.[8] Polarity describes the magnetization direction at the center of the vortex, either up or down. The polarity determines the sense of dynamic vortex core gyration in the in-plane excitation mode.[9]

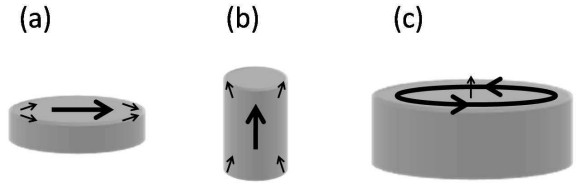

FIG. 1: Schematic illustration of the three basic nanodisk magnetic ground states: (a) in-plane state, (b) out-of-plane state, and (c) vortex state

Determining the phase diagram of magnetic nanodisks is important since this enables one to tailor magnetic material properties and geometry for various possible applications. For example, the single domain in-plane state was used to demonstrate the room temperature magnetic quantum cellular automata (MQCA),[10] and the vortex state has been investigated for potential data storage by switching vortex core polarity.[11,12]

Various micromagnetic simulations[7,13,14] and analytical methods[15,16] have been used to model the magnetic behavior of ferromagnetic nanodisks, and to compute the phase diagram of magnetic ground states (i.e. global energy minimum state) as a function of the diameter and thickness of the nanodisks. Neglecting the Zeeman energy, the total magnetic energy is given by the sum of

the exchange energy, the magnetostatic energy and the magnetocrystalline anisotropy energy:[17]

$$E_{tot} = \int_V \{\frac{A}{M_s^2} \sum_{i=x,y,z} (\nabla M_i)^2 - \frac{\mu_0}{2} \overrightarrow{H_d} \cdot \overrightarrow{M_s} + f_k\} dV \quad (1)$$

Where A is the exchange stiffness, M_s is the saturation magnetization, H_d is the demagnetizing field, and f_k is the magnetocrystalline anisotropy energy density. The exchange interaction favors parallel spin alignment whereas the magnetostatic interaction favors divergence-free spin alignment to reduce the total energy. The total magnetic energy landscape depends on the geometry of the nanodisks (diameter and thickness) and the magnetic properties of the material (saturation magnetization, exchange stiffness, and crystalline anisotropy constant). The magnetic ground state for a given geometry is determined by finding the state with minimum total energy among the possible stable magnetization configurations.

The nanofabrication methods to create magnetic nanodisks include electron beam lithography[18] or nanoimprint lithography[19] followed by lift-off, electrodeposition into templates made by interference lithography,[20] and nanoporous alumina shadow mask technique.[21] Previous measurements to determine the phases of magnetic nanodisks were based on the *average* properties of nanodisk arrays from hysteresis measurement.[7,18] Magnetic domain structure of individual nanodisks also has been observed using magnetic force microscopy (MFM). However, previous imaging works could not determine the nanodisk phase diagram since those studies were often limited to *perpendicularly* magnetized nanodisks,[20,22] or magnetic disks larger than 100 nm in diameter.[19] Determining the phase diagram of magnetic nanodisks has been a challenge for magnetic microscopy since it requires a non-invasive measurement of both the in-plane and out-of-plane magnetization components with high resolution.

In this work, we systematically determine the shape-dependent phase diagram of sub-100 nm disks by measuring the magnetic structure of *individual* nanodisks using high resolution Scanning Electron Microscopy with Polarization Analysis (SEMPA). We observe magnetic configurations based on three distinct ground phases (single domain in-plane, single domain out-of-plane and vortex states) depending on the diameters and thicknesses of the soft magnetic nanodisks. Near the phase boundaries and the triple point, we observe mixtures of different metastable ground phases. Near the boundaries we also observe variations of basic phases, such as tilted vortex states. The magnetic phase diagram generated by using a micromagnetic simulation code agrees qualitatively with the SEMPA observations.

II. EXPERIMENT

To insure that all of the nanodisks were prepared under the same conditions, a single sample with a range of thicknesses and diameters was prepared. Nanodisks of different diameters were defined using electron beam lithography in polymethyl-methacrylate (PMMA) resist. The patterns were generated in an 0.5 mm × 1 mm electron beam exposed area, which was subdivided into 50 μm× 50 μm regions each containing an array of nanodisks of a single diameter as seen in the Scanning Electron Microscope (SEM) image in Fig. 2. A thin Ta film (3 nm) was used as a buffer layer on the Si substrate, and the polycrystalline (Molybdenum)-Permalloy[23] ($Ni_{80}Fe_{15}Mo_5$) wedge film was deposited in an electron beam evaporation chamber under high vacuum conditions (1.2 × 10^{-7} Torr). A linearly varying thickness wedge was generated by using a moving shadow mask during deposition. Lift-off of the unwanted film left behind an array of nanodisks with diameters that ranged from 35 nm to 190 nm and with thicknesses that ranged from 10 nm to 65 nm. The thickness was measured using a calibrated atomic force microscopy (AFM). The array period was designed to be five times larger than the nanodisk diameter so that the magnetostatic interactions between nanodisks are negligible. High magnification SEM images such as those in the inserts in Fig. 2 show that disk diameters were well-defined and uniform even in the smallest disks, however the tallest pillar-like disks were slightly tapered (Figs. 2(b) and 2(d)).

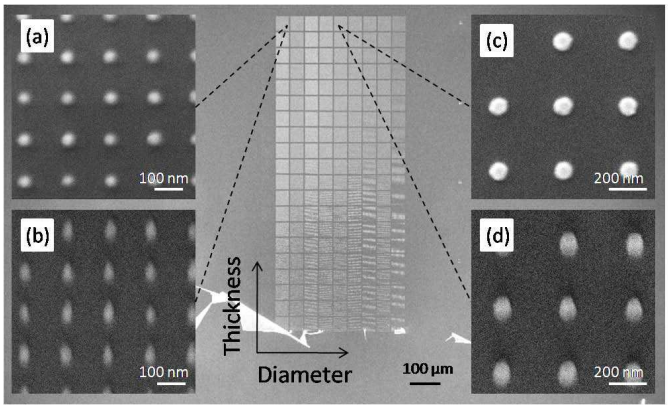

FIG. 2: (a) SEM image showing a low magnification overview of the patterned sample with nanodisk arrays of nine different diameters and continuously varying thickness. The inserts show high magnification images from two arrays acquired at two sample tilts: (a)/(b) 65 nm thick by 35 nm diameter nanodisks, and (c)/(d) 65 nm thick by 90 nm diameter nanodisks. Sample tilt is 0 degree in (a)/(c), and 45 degree in (b)/(d).

SEMPA was used to directly image the in-plane and out-of-plane magnetic structure of the nanodisks. SEMPA measures the magnetization within a few nanometers of the surface by measuring the spin polarization of the emitted secondary electrons.[24,25] As the unpolarized incident electron beam from the field emission SEM is rastered over the sample surface, the topographic image is derived from the secondary electron intensity, while the magnetization image is simultaneously derived from the secondary electron spin polariza-

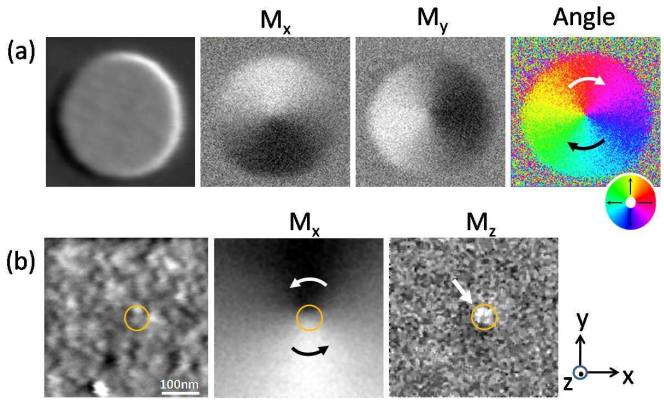

FIG. 3: Examples of SEMPA measurements from 1 μm diameter $\times$ 25 nm thick Permalloy disks. (a) Simultaneously measured images of the topography and the two in-plane (M_x and M_y) magnetization components, and the corresponding, derived in-plane magnetization direction. The magnetization direction is represented by the colors shown in the inset color wheel. (b) Simultaneously measured images of the topography, the in-plane (M_x) and the out-of-plane (M_z) magnetization components from the central region of a disk with opposite chirality. The vortex chirality and polarity can therefore be measured simultaneously.

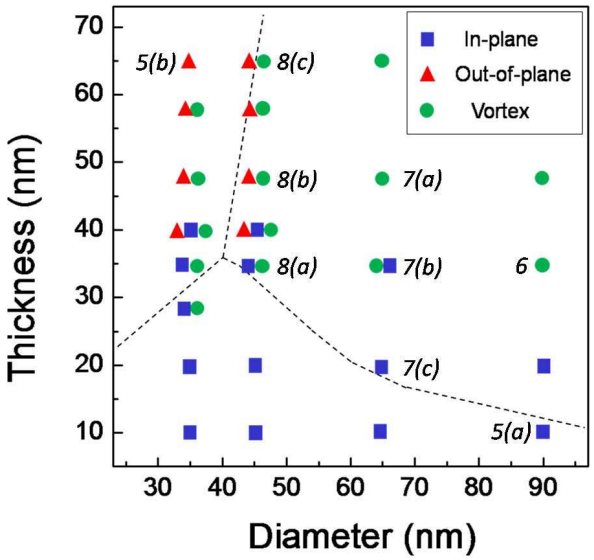

FIG. 4: Summary of the magnetic states observed in SEMPA images as a function of disk size and shape. Disk diameters were either 35 nm, 45 nm, 65 nm, or 90 nm. Near the phase boundaries, multiple grouped symbols indicated that multiple states were observed for the same disk diameter and thickness. The dashed lines are taken from the main phase boundaries calculated by the OOMMF micromagnetic simulations (see Fig. 9(a)) The numbers next to the data points refer to corresponding figures in this paper.

tion, $P = (N_\uparrow - N_\downarrow)/(N_\uparrow + N_\downarrow)$, where $N_\uparrow$ ($N_\downarrow$) are the number of electrons with spins aligned (anti-aligned) with a particular measurement direction. Our spin polarization analyzers can simultaneously measure either the two in-plane magnetization components (M_x and M_y), or one in-plane (M_x) and one out-of-plane (M_z) magnetization component. Examples of SEMPA measurements obtained from 1 μm diameter $\times$ 25 nm thick Permalloy disks are presented in Fig. 3. This disk diameter is somewhat larger than the ones used in this study, but it is still in a single vortex state. The chirality of the vortex state in the disk of Fig. 3(a) is determined by calculating the in-plane magnetization direction from M_x and M_y images , which is represented by the angle image. In fact, the chirality can be determined by just one in-plane component. Fig. 3 (b) shows the topography, in-plane M_x,and out-of-plane M_z images from a disk with opposite chirality. The dark contrast in the upper half and the bright contrast in the lower half of the M_x image in Fig. 3(b) shows that this disk has counter-clockwise chirality. The M_z image shows a small white spot at the center of the vortex. This is a magnetic vortex core with positive polarity. SEMPA can simultaneously measure the chirality and polarity of the vortex. The diameter of the core is about 15 nm and is near the limit of SEMPA resolution. In comparison, the diameters of the smallest disks in this study are 35 nm, so that disks with out of plane magnetization are clearly resolved.

III. RESULTS AND DISCUSSION

We turn now to the SEMPA measurements of the patterned nanodisk sample of Fig. 2 which were carried out at room temperature under ultrahigh vacuum. The sample surface was cleaned by Ar ion bombardment while measuring the surface composition with Auger spectroscopy. The sample was then coated with a 0.5 nm thick Fe film to enhance the magnetic contrast. This Fe film is not thick enough to be ferromagnetic by itself on the bare Si substrate, but it exchange couples to the ferromagnetic elements. In other samples we have studied, the Fe contrast layer did not alter the magnetic domain structure. The probing depth for the spin-polarized secondary electrons is $\approx$1 nm and the incident electron probe diameter is $\approx$10 nm.

The results of all of the SEMPA measurements are summarized in Fig. 4. From the array shown in Fig. 2 we focused on four diameters and nine thicknesses that sample the interesting parts of the phase diagram near the phase boundaries and the triple point. The dashed lines show the phase boundaries obtained from a micromagnetic simulation to be discussed later. The next four figures illustrate the type of data going into the compilation of Fig. 4 including data from some particularly interesting regions of the phase diagram.

The SEMPA magnetization images of Fig. 5 show examples of two of the magnetic ground states, and clearly

demonstrate the striking dependence of the magnetic nanostructure on the nanodisk aspect ratio. Figure 5 shows the SEMPA images of (a) low aspect ratio (90 nm in diameter × 10 nm in thickness) nanodisks with in-plane magnetization, and (b) high aspect ratio (35 nm in diameter × 65 nm in thickness) disks (or pillars) with out-of-plane magnetization. The images correspond to the extreme lower right and upper left points, respectively, in Fig. 4. The images in the first column of Fig. 5 are intensity, and the images in the second and third columns are the corresponding magnetization contrasts measured simultaneously. For in-plane magnetization measurement, by combining the M_x and M_y images, we obtain the direction of the in-plane magnetization or angle, $\theta_{xy} = tan^{-1}(M_y/M_x)$. Figure 5(a) shows weak M_x contrast and dark M_y contrast, and the combined angle image is represented in color with directions given by a color wheel. The calculated value for the surface magnetization direction is 228±5 degrees (0 degree corresponds to the red direction). Note that an independent measurement of M_z on these disks did not show any magnetic contrast. However, the nanodisks with high aspect ratio, that is nanopillars, show either bright or dark out-of-plane magnetization as in the M_z image of Fig. 5(b). Surprisingly, the magnetization in the surface region measured by SEMPA also has a significant in-plane, M_x, component as well as an out-of-plane, M_z component. This corresponds to a surface magnetization that is tilted into or out of plane by 30±10 degrees with respect to the surface. The color wheel for Fig. 5(b) corresponds to $\theta_{xz} = tan^{-1}(M_z/M_x)$. We speculate that the observed in-plane magnetization component may be due to tilting of the surface magnetization in order to reduce the magnetostatic energy at the top surface. The resulting magnetic configuration would be out-of-plane state with curling of magnetization near the top surface. This is reminiscent of an asymmetric surface Néel wall cap on an interior Bloch wall which minimizes the surface magnetostatic energy in the bulk sample.[26]

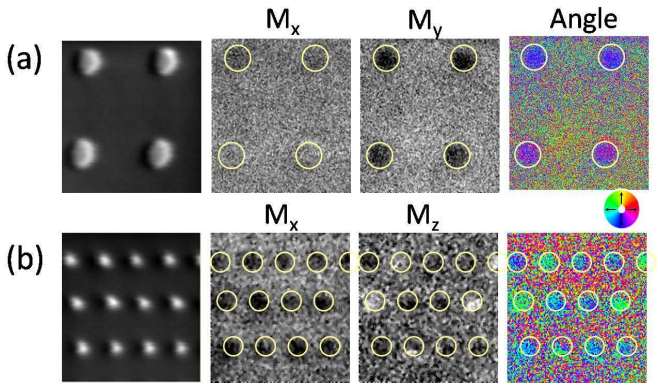

FIG. 5: SEMPA images of (a) in-plane magnetic states in 90 nm diameter × 10 nm thick disks, and (b) out-of-plane magnetic states in 35 nm diameter × 65 nm thick disks. Simultaneous measured topography and either two in-plane, or one in-plane and the out-of-plane magnetization components are shown. From these components, the in-plane magnetization angle (a), and the out-of-plane magnetization tilt angle in the M_x and M_z plane (b) were derived. Note that the out-of-plane magnetic structure has a significant in-plane component which may indicate curling of magnetization near the top surface.

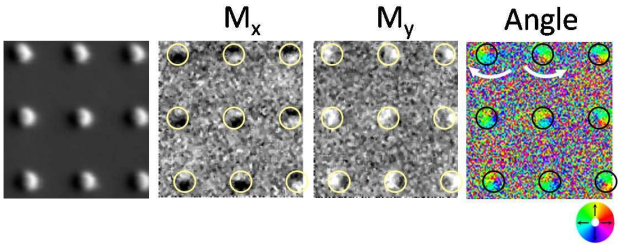

FIG. 6: SEMPA images of vortex magnetic states in 90 nm diameter × 35 nm thick disks. The in-plane magnetization direction is represented by the inset color wheel. The array contains vortex states with two different chiralities.

The SEMPA magnetization images of Fig. 6 for nanodisks with a diameter of 90 nm and a thickness of 35 nm present a clear example of the third nanodisk magnetic ground state, a vortex state. The M_x and M_y components have both dark and bright contrast present within each nanodisk that is characteristic of a magnetic vortex state. Furthermore, from the derived in-plane magnetization angle image shown in Fig. 6 one can see that both of the two possible chiralities of magnetic vortex are present in this nanodisk array. We did not attempt to measure the vortex core polarity for these nanodisks.

Near the phase boundaries and the triple point, it is not unusual to find multiple different phases present simultaneously. The series of the SEMPA images in Fig. 7 shows the transition from the vortex phase to the in-plane phase, and the mixture of the two ground phases near the phase boundary, for 65 nm diameter nanodisks as the thickness decreases from (a) 48 nm, (b) 35 nm, to (c) 20 nm. In Fig. 7(a), all the nanodisks show dark/bright contrast indicating vortex magnetization. However, in Fig. 7(b), the nanodisks in the first row show uniform contrast, while the rest of the nanodisks in the array show dark/bright contrast. This indicates a mixture of the in-plane state and the vortex state in the 65 nm in diameter × 35 nm in thickness nanodisk array. In Fig. 5(c), all the nanodisks but the one at the bottom left corner shows uniform bright contrast representing the in-plane state. We note that the simultaneous measurements of the Mz component in these disks have no magnetic contrast (not shown).

Figure 8 shows a series of the SEMPA images of Permalloy nanodisks with the same 45 nm diameter near the out-of-plane to vortex phase boundary. This slice through the phase diagram is interesting both for the presence of multiple states near the phase boundary, and the existence of complex states that are some combination of the three basic magnetic phases. The images of

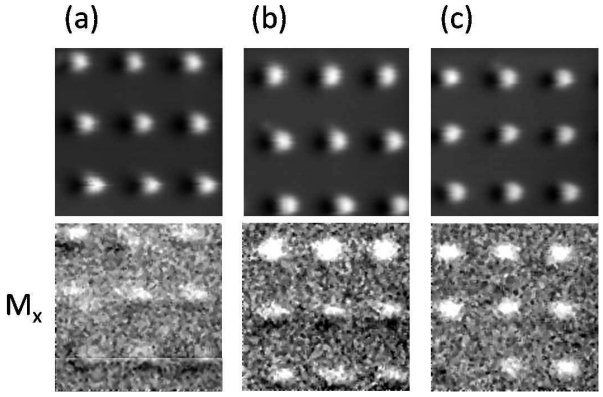

FIG. 7: SEMPA images which show the transition with decreasing thickness from a vortex state in (a) to an in-plane state in (c). Disk thicknesses were (a) 48 nm thick, (b) 35 nm thick, and (c) 20 nm thick. Disk diameters were all 65 nm. In (b), a mixture of the two ground phases is observed near phase boundary.

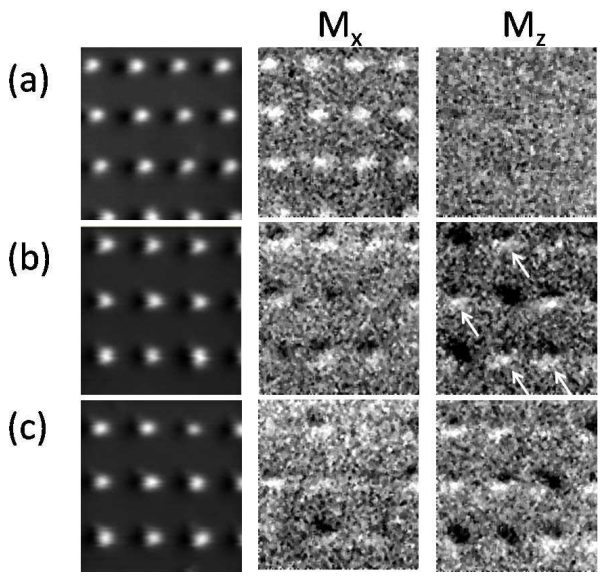

FIG. 8: SEMPA images of disks with sizes along the out-of-plane/vortex phase boundary. Disk thicknesses were (a) 35 nm, (b) 48 nm, and (c) 65 nm. Disk diameters were all 45 nm. In addition to showing the transition from (a) in-plane state to (c) out-of-plane state with increasing thickness, the images also reveal more complex magnetic states such as the tilted vortex states indicated by arrows in (b).

nanodisks, which are (a) 35 nm thick, (b) 48 nm thick, and (c) 65 nm thick, show the transition from the in-plane state to complex out-of-plane states with increasing thickness. For thin nanodisks the surface magnetization is in-plane (Fig. 8(a)), whereas images of the thick nanodisks show stronger out-of-plane magnetization contrast (Fig. 8(c)). However, in the intermediate case (Fig. 8(b)), the nanodisks have uniform or dark/bright contrasts in both M_x and M_z components. Interestingly, some nanodisks have dark/bright contrast both in-plane and out-of-plane magnetization (see arrows in Fig. 8(b)). While the dark/bright contrast in the in-plane component indicates a vortex state, the dark/bright contrast in the out of plane component is consistent with a vortex that is tipped with respect to the surface plane. Thus in this crossover region of the phase diagram we observe a *tilted* vortex magnetization state that is a magnetization configuration intermediate between the three ground phases. The tilting angle determined from M_x and M_z values in areas of maximum contrast is 55 ± 7 degrees with respect to the surface plane. Near the triple point, the SEMPA measurement also showed the coexistence of different ground phases and complex tilted phases, but some nanodisks did not have significant magnetic contrast in either M_x or M_z components, which made them difficult to interpret.

The magnetic ground states of isolated Permalloy nanodisks with different geometries were calculated using the OOMMF micromagnetic simulation code with edge corrections.[27,28] The material parameters used for Permalloy were the saturation magnetization $M_s = 8.0\times 10^5$ A/m and the exchange stiffness $A = 1.3\times10^{-11}$ J/m. The crystalline anisotropy was neglected. The unit cell size for the three dimensional simulation was 1 nm $\times$ 1 nm $\times$ 1 nm, which is much smaller than the exchange length of Permalloy ($l_{ex} \approx 5.7$ nm). The magnetic behavior of a Permalloy nanodisk is closely related to the magnetic exchange length, which in turn can be used to normalize the geometric dimensions in the phase diagram.

Micromagnetic calculations were carried out using different initial states. For each nanodisk geometry separate energy minimizations were carried out starting from vortex-like, in-plane-like and out-of-plane-like initial states. In each case, the initial states were made slightly asymmetric to ensure that the resulting states were stable. From these equilibrium states, the ground state phase diagram was determined by selecting the state with the smallest energy. The bistable regions of the phase diagram were determined by noting which sample dimensions resulted in more than one equilibrium state.

Figure 9(a) shows the phase diagram of magnetic ground states of Permalloy nanodisks simulated as a function of the disk diameter and thickness. The phase diagram shows the three phases (the in-plane, the out-of-plane, and the vortex state) and the approximate phase boundaries. The different phases are represented by the out-of-plane (M_z) component of magnetization in the plot. The in-plane phase has $M_z \approx 0$ and the out-of-plane phase has $M_z \approx 1$. The vortex phase shows decreasing M_z with increasing diameter. The triple point of the three phases is also shown at the diameter of $\sim$40 nm and the thickness of $\sim$35 nm. In terms of M_z, the transition from the in-plane state to the out-of-plane state or from the in-plane state to the vortex state is discontinuous. In particular, the phase boundary between the

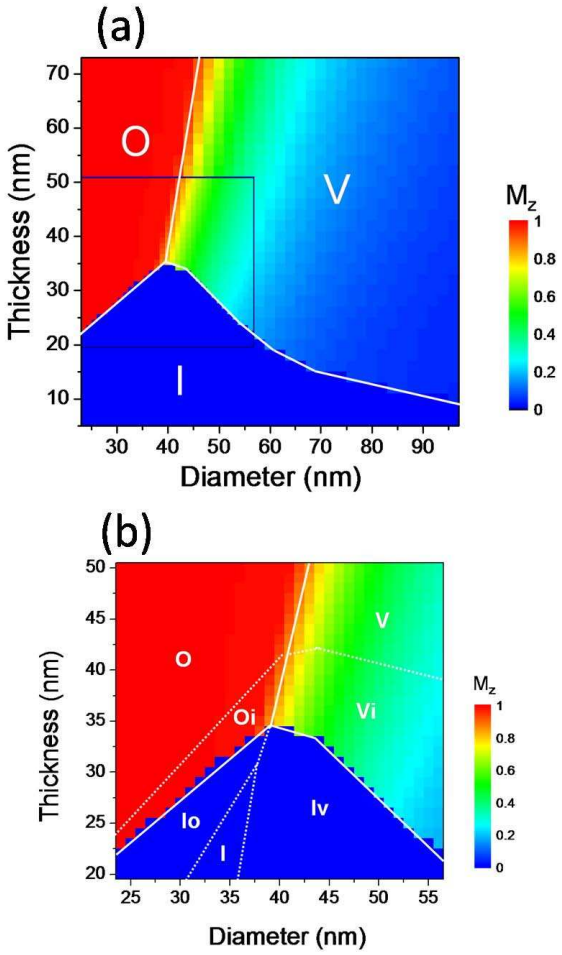

FIG. 9: Nanodisk magnetic state phase diagrams derived from OOMMF micromagnetic simulations. The phase diagrams show the boundaries between the three basic phases (in-plane: **I**, out-of-plane: **O**, vortex phase: **V**), and the color-coded, normalized out-of-plane magnetization component (M_z). (a) Main phase boundaries (solid lines) between minimum energy ground states. (b) Metastable phase boundaries (dashed lines) near the triple point (boxed region in (a)) that arise when more than one stable state was found. In the metastable regions the capital letters correspond to the magnetic ground phase, while the small letters represent metastable phases.

in-plane and the out-of-plane states is close to the aspect ratio of ≈0.9, which is in good agreement with the analytical calculation by assuming the uniform demagnetization factor[29] and quasiuniform magnetization state.[30] In contrast, M_z varies continuously in the transition from the out-of-plane state to the vortex state, with an abrupt change in the slope of M_z vs. diameter at the phase boundary. Moving away from this phase boundary with increasing diameter, the vortex state develops from the out-of-plane state as the magnetization around the circumference of the disk twists and tilts towards the in-plane direction leaving vertically oriented magnetization in the vortex core.

The phase boundary corresponds to the nanodisk geometry where the total energies of two different phases are equal. As a consequence, the minimum energy density is continuous across the phase diagram, exhibiting cusps in the energy density as each of the phase boundaries is crossed. The exchange energy is the largest component of the total energy in the vortex region, and the magnetostatic energy is dominant in the in-plane and the out-of-plane region. The phase boundary between the in-plane and out-of-plane states has the highest energy density.

Regions of bistability, where more than one stable state was calculated, are shown in Fig. 9(b). Bistable regions occur near the in-plane to vortex phase boundary and near the in-plane to out-of-plane phase boundary. No bistability was found near the out-of-plane to vortex phase boundary. In passing, we note that the bistability is only observed at phase boundaries where the magnetization pattern changes discontinuously. The existence of metastable states near the phase boundary was described recently by an analytical calculation[31] and was also demonstrated experimentally.[32,33]

The existence of metastable states along phase boundaries can partly explain the mixture of ground states near the phase boundaries that were observed by SEMPA. Furthermore, in those regions near the phase boundaries, we speculate that the stable states of each individual nanodisk may depend more strongly on the small variations in the nanodisk geometry, grains, defects, and surface and edge roughness than in the regions far from the phase boundaries.

The SEMPA measurements revealed states that were not predicted from the micromagnetic calculations. Neither the in-plane surface magnetization on the out-of-plane state shown in Fig. 5(b) nor the tilted vortex state shown in Fig. 8(b) were observed in the micromagnetic calculations. Initial states mimicking a tilted uniform state or a tilted vortex state proved to be unstable in the cylinder geometry. These unexpected magnetic states may be due to deviations from the ideal cylindrical geometry, and should therefore be most likely for the smallest, and therefore most lithographically challenging disk shapes. However, stable tilted vortex states have been calculated in a cubic geometry.[34]

IV. CONCLUSIONS

In conclusion we have measured the Permalloy nanodisk magnetic state phase diagram by using SEMPA to directly image the in-plane and out-of-plane magnetic structure of nanodisks with different diameters and thicknesses. We determined the phase boundaries and the triple point between the three basic magnetic states: in-plane, out-of-plane, and vortex. Near the phase boundaries and the triple point, however, multiple ground states or complex metastable states are observed in nanodisks with nominally identical dimensions. Note

that these states would have been very difficult to identify from non-spatially resolved measurements of average magnetic properties of the disk arrays. The magnetic phase diagram computed from OOMMF micromagnetic simulations showed a good qualitative agreement with the phase diagram determined by the SEMPA measurement. However, a few structures, such as tilted vortex states, were observed that were not predicted by the modeling; possibly due to deviations from ideal geometries. Finally, we note that by scaling the results using appropriate exchange lengths, these measurements of nanodisk magnetic phases in the sub-100 nm regime can also be applied to determining the magnetic phases for nanostructures with different materials and shapes. This result will enable tailoring material properties and geometry of nanostructures for various potential applications.

Acknowledgments

This work is supported by the NIST-CNST/UMD-NanoCenter Cooperative Agreement. Research performed in part at the NIST Center for Nanoscale Science and Technology. We are grateful to T. Clinton for stimulating discussions.

[1] S. A. Wolf, A. Y. Chtchelkanova, and D. M. Treger, IBM J. Res. & Dev. **50**, 101 (2006).
[2] S. Y. Chou, Proc. IEEE **85**, 652 (1997).
[3] S. Parkin, J. Xin, C. Kaiser, A. Panchula, K. Roche, and M. Samant, Proc. IEEE **91**, 661 (2003).
[4] D. C. Ralph, and M. D. Stiles, J. Magn. Magn. Mater. **320**, 1190 (2008).
[5] E. Feldtkeller and H. Thomas, Phys. Kondens. Mater. **4**, 8 (1965).
[6] A. Hubert and R. Schafer, Magnetic Domains - the Analysis of Magnetic Microstructures, Springer, Berlin (1998).
[7] C. A. Ross, M. Hwang, M. Shima, J. Y. Cheng, M. Farhoud, T. A. Savas, H. I. Smith, W. Schwarzacher, F. M. Ross, M. Redjdal, and F. B. Humphrey, Phys. Rev. B **65**, 144417 (2002).
[8] K. Y. Guslienko, V. Novosad, Y. Otani, H. Shima, and K. Fukamichi, Phys. Rev. B **65**, 024414 (2001).
[9] S.-B. Choe, Y. Acremann, A. Scholl, A. Bauer, A. Doran, J. Stohr, and H. A. Padmore, Science **304**, 420 (2004).
[10] R. P. Cowburn, and M. E. Welland, Science **287**, 1466 (2000).
[11] B. Van Waeyenberge, A. Puzic, H. Stoll, K. W. Chou, T. Tyliszczak, R. Hertel, M. Fähnle, H. Brückl, K. Rott, G. Reiss, I. Neudecker, D. Weiss, C. H. Back, and G. Schütz, Nature **444**, 461 (2006).
[12] K. Yamada, S. Kasai, Y. Nakatani, K. Kobayashi, H. Kohno, A. Thiaville, and T. Ono, Nat. Mater. **6**, 270 (2007).
[13] W. Scholz, K. Yu. Guslienko, V. Novosad, D. Suess, T. Schrefl, R. W. Chantrell, and J. Fidler, J. Magn. Magn. Mater. **266**, 155 (2003).
[14] J. K. Ha, R. Hertel, and J. Kirschner, Phys. Rev. B **67**,224432 (2003).
[15] K. L. Metlov, and K. Yu. Guslienko, J. Magn. Magn. Mater. **242**, 1015 (2002).
[16] P. O. Jubert, and R. Allenspach, Phys. Rev. B **70**, 144402 (2004).
[17] W. F. Brown, Micromagnetics, Wiley, New York (1963).
[18] R. P. Cowburn, D. K. Koltsov, A. O. Adeyeye, and M. E. Welland, Phys. Rev. Lett. **83**, 1042 (1999).
[19] I. L. Prejbeanu, M. Natali, L. D. Buda, U. Ebels, A. Lebib, Y. Chen, and K. Ounadjela, J. Appl. Phys. **91**, 7343 (2002).
[20] C. A. Ross, M. Farhoud, M. Hwang, H. I. Smith, M. Redjdal, and F. B. Humphrey, J. Appl. Phys. **89**, 1310 (2001).
[21] J. Meja-Lpez, D. Altbir, A. H. Romero, X. Batlle, I. V. Roshchin, C. Li, and I. K. Schuller, J. Appl. Phys. **100**, 104319 (2006).
[22] G. D. Skidmore, A. Kunz, C. E. Campbell, and E. D. Dahlberg, Phys. Rev. B **70**, 012410 (2004).
[23] R. M. Bozorth, Ferromagnetism, D. Van Nostrand Company, Inc., New York (1951).
[24] M. R. Scheinfein, J. Unguris, M. H. Kelley, D. T. Pierce, and R. J. Cellota, Rev. Sci. Instrum. **61**, 2501 (1990).
[25] J. Unguris, "SEMPA and its Applications," in Experimental Methods in the Physical Sciences 36, eds. M. De Graef and Y. Zhu, Academic Press, New York (2001) p. 167-194.
[26] M. R. Scheinfein, J. Unguris, R. J. Celotta, and D. T. Pierce, Phys. Rev. Lett. **63**, 668 (1989).
[27] M. J. Donahue, and D. G. Porter, Interagency Report NISTIR 6376, National Institute of Standards and Technology, Gaithersburg, MD (Sept. 1999).
[28] M. J. Donahue and R. D. McMichael, IEEE Trans. Mag. **43**, 2878 (2007).
[29] A. Aharoni, J. Appl. Phys. **68**, 2892 (1990).
[30] K. L. Metlov, and K. Yu. Guslienko, Phy. Rev. B **70**, 052406 (2004).
[31] K. L. Metlov, and Y. P. Lee, Appl. Phys. Lett. **92**, 112506 (2008).
[32] H.F. Ding, A. K. Schmid, D. Li, K. Yu Guslienko, and S. D. Bader, Phys. Rev. Lett. **94**, 157202 (2005).
[33] A. V. Jausovec, G. Xiong, and R. P. Cowburn, J. Appl. Phys. **99**, 08B103 (2006).
[34] M. J. Donahue, private communication.